




## Article

# Tribocorrosion-Resistant Surface for TiO<sub>2</sub> as a Function of Load and Sliding Speed

Jorge Bautista-Ruiz <sup>1,\*</sup>, Willian Aperador <sup>2</sup> and Jorge Sánchez-Molina <sup>1</sup>

<sup>1</sup> Centro de Investigación de Materiales Cerámicos, Universidad Francisco de Paula Santander, San José de Cúcuta 540003, Colombia

<sup>2</sup> Department of Engineering, Universidad Militar Nueva Granada, Bogotá 110111, Colombia

\* Correspondence: jorgebautista@ufps.edu.co

**Abstract:** The applications projected in the coatings are in implants with the lower extremities since they require a great load capacity and are essential for walking. Therefore, the use of devices or implants is necessary for recovery, osteosynthesis, and fixation. The tribocorrosive behavior of nanostructured compounds based on titanium oxide with an intermediate layer of gold deposited on titanium substrates was determined. These coatings were obtained using the reactive magnetron sputtering technique. Tribocorrosive properties were evaluated at sliding speeds of 3500 mm/min, 4500 mm/min, 6000 mm/min, 7500 mm/min, and 9000 mm/min with loads of 1 N, 2 N, 3 N, 4 N, and 5 N. The coatings were characterized by X-ray photoemission spectroscopy and X-ray diffraction, and the surface roughness was analyzed by atomic force microscopy. The dual mechanical and electrochemical wear tests were carried out with a potentiostat coupled to a pin on the disk system. The system was in contact with a hanks solution (37 °C), which acted as a lubricant. Structural characterization made it possible to identify the TiO<sub>2</sub> compound. In the morphological characterization, it was found that the substrate influenced the surface properties of the coatings. The tribological behavior estimated by the wear rates showed less wear at higher load and sliding speeds. It was shown that it is possible to obtain coatings with better electrochemical and tribological performance by controlling the applied load and slip speed variables. In this study, a significant decrease corresponding to 64% was obtained, specifically in the speed of deterioration, and especially for a load of 5 N, depending on the sliding speed that went from 0.2831 mpy (Mils penetration per year) to 3500 mm/min compared to 0.1045 mpy at 9000 mm/min, which is explained by the mechanical blockage induced by the coating.



**Citation:** Bautista-Ruiz, J.; Aperador, W.; Sánchez-Molina, J. Tribocorrosion-Resistant Surface for TiO<sub>2</sub> as a

Function of Load and Sliding Speed.

*Lubricants* **2023**, *11*, 91. <https://doi.org/10.3390/lubricants11030091>

Received: 10 January 2023

Revised: 3 February 2023

Accepted: 16 February 2023

Published: 21 February 2023



**Copyright:** © 2023 by the authors. Licensee MDPI, Basel, Switzerland. This article is an open access article distributed under the terms and conditions of the Creative Commons Attribution (CC BY) license (<https://creativecommons.org/licenses/by/4.0/>).

**Keywords:** thin films; titanium oxide; gold; corrosion; tribology

## 1. Introduction

Studies carried out from the biomedical point of view have determined favorable conditions of biocompatibility in titanium implants. When titanium oxidizes, it generates a thin superficial layer of TiO<sub>2</sub> due to the passivation process when it comes into contact with aqueous media, such as physiological solutions. However, additional conditions are necessary to improve the oxide layer's effectiveness. Therefore, it is necessary to apply vacuum heat treatments to the material [1]. It has also been found that the thin layer of TiO<sub>2</sub> (in the order of nanometers) is responsible for titanium implants' high degree of biocompatibility and allows the neutralization of free radicals that are produced in inflammatory processes. This evaluation was carried out on surfaces with thicknesses between 5 and 100 μm [2]. New research should focus on reducing the thickness of the layers in order to avoid the dimensional modification of parts to be replaced. The magnetron sputtering technique is ideal for this application because it allows coatings with good adherence to be obtained and the need for intermediate gold layers to block the passage of ions to the substrate. Other advantages of the magnetron sputtering technique are the growth of

coatings with thicknesses less than 5  $\mu\text{m}$  and good mechanical properties. Although it has been in production for several decades, thin-film technology is still under development. Everyday advances are presented in the techniques for producing thin films by physical vapor deposition PVD, which are based on the study of the conditions for obtaining them and the formulation of optimal stoichiometries to generate effective materials [3].

The action of tribology is related to joint replacements due to the characterization of the behavior of the implant, evaluating the factors that affect its useful life [4]. In the case of hip or knee joint replacements, phenomena such as wear or corrosion can lead to the loss of the prosthesis [5]. These phenomena can coincide or be in isolation in everyday situations, such as standing up, performing physical activities, or walking. Gait speeds in an average person can vary depending on factors such as anthropometric measurements, age, gender, and external factors related to the terrain, type of footwear, and if the person carries any load. However, under normal conditions, walking speeds are classified into three types: low, medium, and high speeds, which are also characterized by a range from 0.8 to 1.5 m/s in an average person [6]. On the other hand, the loads on the hip or knee can vary depending on the person's walking position. These factors are relevant because they are the starting point for studying the possible wear that joint replacements may present [7].

There are several studies involving titanium and gold. It is possible to cite a new method to improve the biofunctionalization of Ti materials by immersing them in gold-sprayed titanium plates [8]. This is alongside exhibiting antibacterial properties and influencing the processes of osteoblast cell growth [9–12], the osseointegration of dental implants [13], the use of  $\text{TiO}_2$  [14,15] in photoactivity, and the study of the effect of gold coating on porcelain adhesion [16].

In biological systems, orthopedic implants are subjected to repetitive cycles, generating mechanical wear on the material's surface. In most cases, two or three bodies are in contact, causing abrasive, adhesive, friction, or even fatigue wear [17]. These unwanted factors in the human body alter the balance of the system by presenting aseptic loss due to the detachment of particles, causing an inflammatory response (osteolysis) and the loss of the implant. In addition, to wear, corrosion leads to accelerated degradation due to chemical processes generated on the implant surface. Phenomena such as pitting corrosion (crevice corrosion), intergranular corrosion, or fatigue corrosion release ions that can cause damage at a cellular level, the appearance of tumors, and damage to the surrounding tissues [18,19].

Wear and corrosion are also destructive mechanisms affecting the valuable life of orthopedic implants. The wear and formation of harmful particles occur in artificial joints that impact the wearer's performance and health. Furthermore, when the metallic parts of implants are exposed to body fluids, they become oxidized and generate corrosion products, affecting the implant and causing health risks [20]. Titanium alloys are widely used in the biomedical industry due to their excellent mechanical properties, corrosion resistance, and cytocompatibility. However, unfortunately, the tribological properties are poor, and the shelf life in the human body is limited. Therefore, the development of coatings that protect materials from degradation and improve useful life is required [20].

This work studied the synergy between wear and corrosion as a cause of failure in metallic implants and as a function of variables such as the applied load, sliding speed, wear rate, and corrosion rate. In addition, the performance of the material that covers the titanium applied in biomaterials was characterized. For the evaluation of the behavior of the  $\text{TiO}_2$  films, tribology and corrosion tests were applied under simulated biological fluid conditions (Hank's solution).

## 2. Materials and Methods

The films were obtained in a magnetron sputtering RF. The equipment consisted of a stainless-steel chamber with working pressures close to  $10^{-7}$  Torr, a controlled atmosphere generation system, a vacuum system made up of a mechanical pump, and a turbo-molecular pump connected in series. The Pirani-type pressure sensor with a 1-inch diameter magnetron was located above the target, and a 13.56 MHz RF source with impedance matching.

Titanium targets with a 4-inch diameter of 99.9% purity were used. The constant parameters were 50 W of power, a working pressure of  $2.6 \times 10^{-3}$  mbar, and a substrate temperature of 300 °C. Variation in the oxygen percentage at 12.5%, 25%, 37.5%, and 50% took place in the Ar/O<sub>2</sub> gas mixture. Gold films approximately 800 nm thick were deposited at room temperature with an 80-rpm rotation of the substrate, 150 W DC power in the gold target, and a time of 20 min. The thickness of the TiO<sub>2</sub> films was approximately 1600 nm.

XPS experiments were carried out in a SPECS Sage HR 100 spectrometer with a non-monochromatic X-ray source (Magnesium K $\alpha$  line of 1253.6 eV energy). Power was applied at 250 W and calibrated using the 3d<sub>5/2</sub> range of Ag with a full width at a half maximum (FWHM) of 1.1 eV. The selected resolution for the spectra was 15 eV of pass energy and 0.15 eV/step. All measurements were performed under an ultra-high vacuum (UHV) chamber at a pressure of around  $8 \times 10^{-6}$  Pa. The samples were assessed subsequently to the deposition with the PVD technique.

The X-ray diffraction technique used an EMPYREAN-PANalytical unit with Cu-K $\alpha$  monochromatic radiation and a wavelength of 1.5406 Å. Bragg-Brentano geometry, goniometer in  $\theta/\theta$  configuration, a  $2\theta$  range between 10° and 90°, and a step and step time of 0.02° and 2 s were also used, respectively. In the mineralogical characterization, the different crystalline phases were identified by comparing the particular diffractions of the spectra obtained with the spectra of the COD-2022 database (crystallography open database).

Before the wear tests, the surfaces of the samples were analyzed by atomic force microscopy (AFM), in an area of 45  $\mu\text{m} \times 45 \mu\text{m}$ , in the contact mode and using Asylum Research model MFP-3D equipment. A Carl Zeiss LSM 700 Laser scanning confocal microscope (LSCM) was used in the topographical characterization of the worn surfaces.

For the evaluation of the tribocorrosion tests, the radius of the track was 0.003 m, and the travel distance was 50 m. The selected pin is made of bone with a pin diameter of 0.004 m and a rounded head. The pin was made from a bovine femur head. Hank's solution was used for the tests in simulated biological fluid. The equipment on which the tribology tests were carried out was a nanovea T100 tribometer. The selected speeds were 3000, 4500, 6000, 7500, and 9000 mm/min with loads of 1, 2, 3, 4, and 5 N.

The surface roughness of the samples was measured on the Ra scale by AFM and using AFM-Nanosurf Easyscan 2 STM equipment.

### 3. Results

#### XPS

The electronic properties of the gold adhesive layer-type coatings and the TiO<sub>2</sub> functional coating were evaluated by X-ray photoemission spectroscopy [21]. Figure 1 shows the gold coating 4F<sub>5/2</sub> y and gold coating 4F<sub>7/2</sub> bonds at 87.92 eV and 84.26 eV, respectively. This result provides evidence of the non-existence oxidation of the deposited gold [12].

Figure 2 shows the spectrum of the TiO<sub>2</sub> components deposited on a gold layer. The interaction between gold and TiO<sub>2</sub> at the interface is evident. In the spectrum, signals corresponding to plasmonic loss and associated with TiO<sub>2</sub> were obtained at 471 eV and 477 eV. The peaks located at 464 eV and 458 eV are related to the orbital spin Ti2p<sub>3/2</sub> y Ti2p<sub>5/2</sub>. These photoelectron peaks are attributed to the elements of titanium and oxygen [22]. Stoichiometrically relates two oxygen atoms bonded to a titanium atom and corresponds to the characteristic ionization of oxygen located as a vacancy in the crystal structure, generating a region that stoichiometrically corresponds to oxidation.

Figure 3 shows the XRD spectrum of the gold coating. The structural parameters were calculated by Rietveld refinement [23]. By employing the letter JCPDF 040784, its correspondence with the gold compound was determined. In the spectrum, Bragg reflection peaks were observed at 38.20° and indexed in the (111) planes and 81.90° corresponding to the crystallographic plane (222), for which it is established that it corresponds to crystalline gold with high purity. Gold has an FCC structure with lattice parameters  $a = b = c = 4.0786 \text{ \AA}$  and angles  $\alpha = \beta = \gamma = 90^\circ$ .

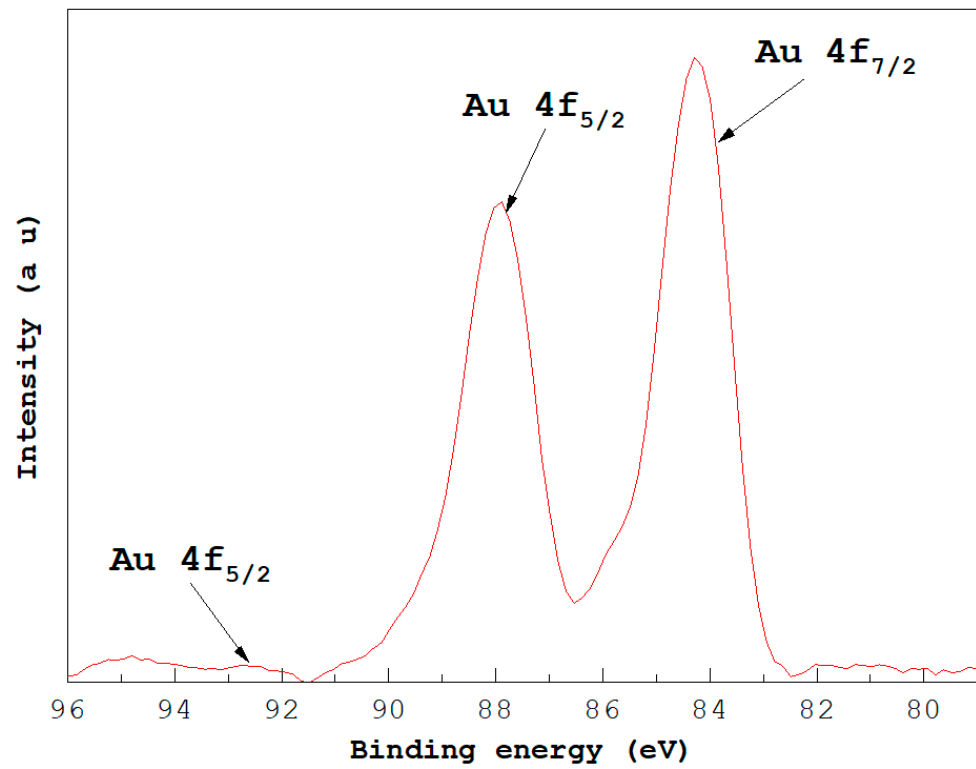


Figure 1. XPS spectrum corresponding to gold coating.

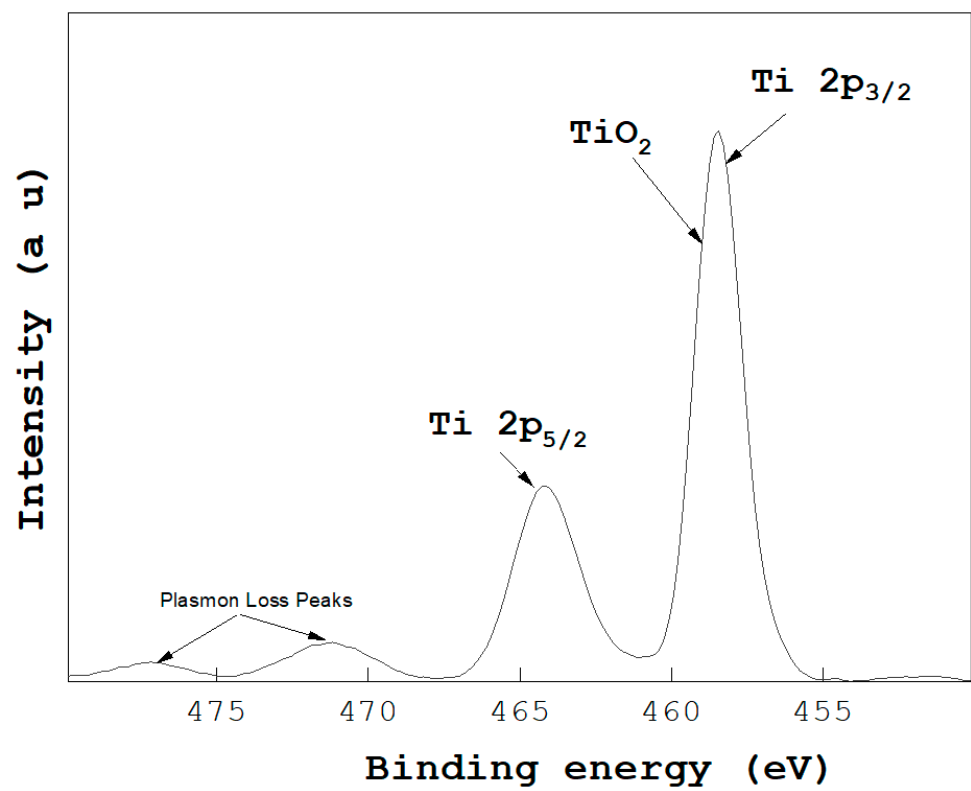
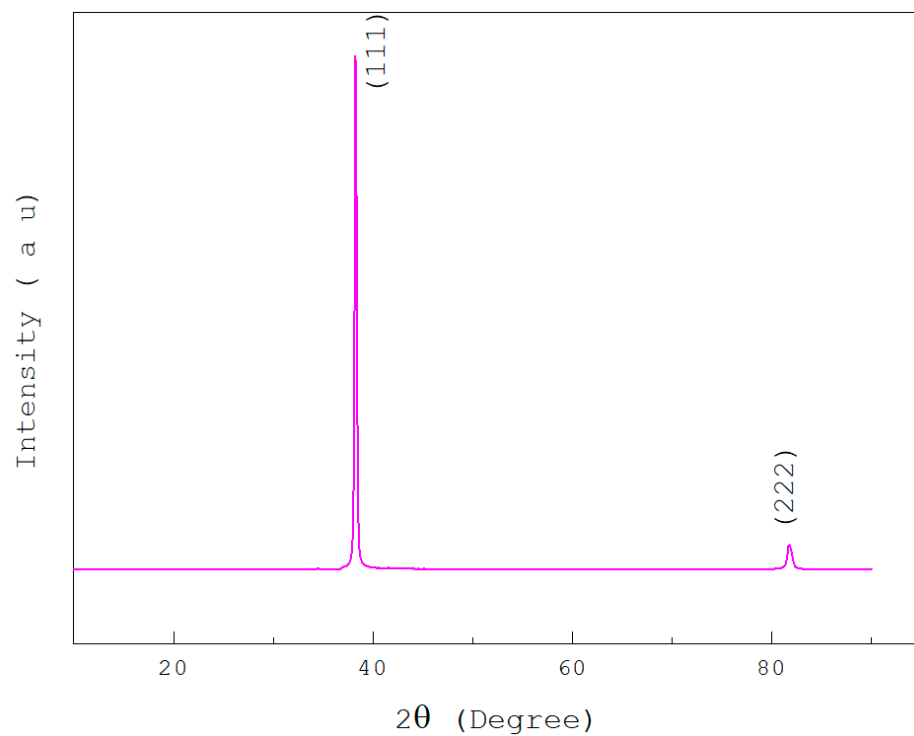
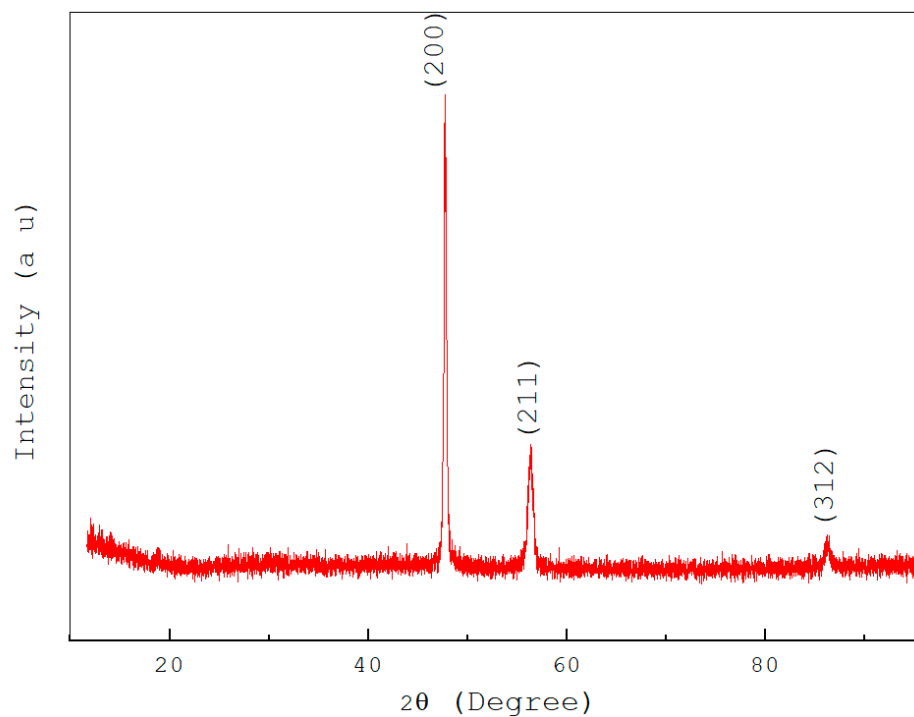


Figure 2. XPS spectrum corresponds to titanium oxide coating.



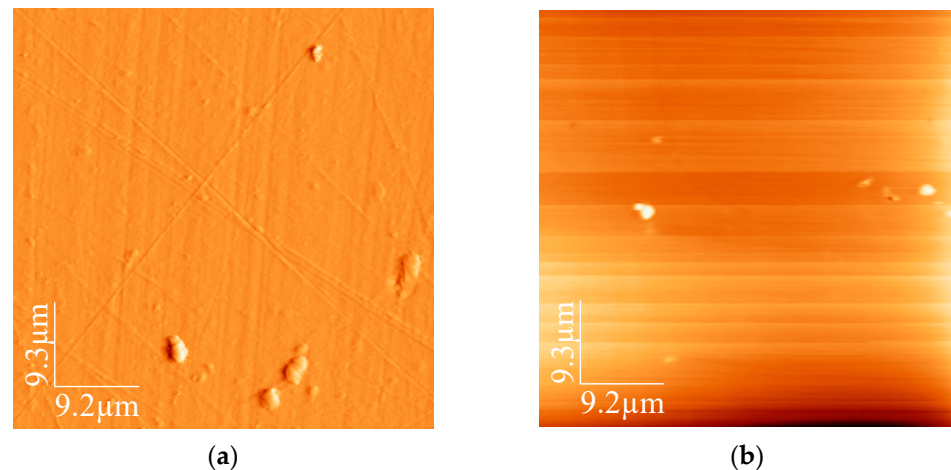
**Figure 3.** X-ray diffraction spectrum of the intermediate layer of gold located between the substrate and the TiO<sub>2</sub> coating.

Figure 4 shows the X-ray diffraction spectrum of the TiO<sub>2</sub> compound deposited on the (intermediate) layer of gold. In the diffractogram, peaks ( $2\theta = 47.81^\circ$ ) indexed in (200) planes,  $56.36^\circ$  indexed in (211) planes, and  $2\theta = 86.33^\circ$  indexed in the (312) planes are identified. They confirm the TiO<sub>2</sub> compound according to the crystallographic base JCPDF 211,276 [24]. TiO<sub>2</sub> is the only crystalline compound present [25].



**Figure 4.** X-ray diffraction spectrum for TiO<sub>2</sub> coating.

Figure 5 shows the gold (Figure 5a) surface topography and TiO<sub>2</sub> (Figure 5b) coatings [26]. The gold coating shows a heterogeneous surface where well-defined areas associated with the preparation process of the titanium substrate are evident. The two-dimensional image of the sample (Figure 5a) shows changes in surface roughness due to particle growth. The roughness values were determined at  $4.7 \pm 0.2$  nm. The surface of the TiO<sub>2</sub> coating was rougher than that of the gold surface [27]. On this surface, the growth of particles with varied sizes ordered as a “chain” was observed. As a result, the roughness value of the TiO<sub>2</sub> coating was  $7.6 \pm 0.8$  nm.



**Figure 5.** Topographic images obtained by atomic force microscopy. (a) Gold coating and (b) TiO<sub>2</sub> coating.

The surface roughness values of the system were made up of a substrate-gold layer-TiO<sub>2</sub> layer that allowed characterization in the study region. It can be observed in the AFM images obtained (Figure 5) that the changes in the sample surface were characterized by slight growths of the grains due to the application of the gold film to generate the adhesion of the titanium oxide layer. When the coating had all the layers, regions marked by a plate-like growth were observed. Low roughness values in the gold sample are likely due to the re-evaporation process of the material, which reduces the possibility of the agglomeration of the grains during growth. The nucleation processes associated with the formation of grains on the surface are the product of the reactions of the precursor species during the deposition stage.

Figure 6 shows the potentiodynamic polarization curves of the TiO<sub>2</sub> coatings when evaluated at different sliding speeds and applied loads of 1 N, 2 N, 3 N, 4 N, and 5 N, respectively. The potentiodynamic curves, Hanks' solution with pH = 7.4, and 37 °C temperature were used as the electrolyte [28,29]. The results allowed the coatings presented at a low current density and noble corrosion potential to be deduced as behavior that was evident in the coatings with increasing loads [30]. The trend of the potentiodynamic polarization curves indicated the formation of a durable film. In addition, as the anodic branch advanced, a zone between 0 mV and 150 mV vs. Ag/AgCl was observed where the coating material tried to passivate. Although there was an irregularity in the behavior, the presence of localized corrosion phenomena was not revealed. In all the cases evaluated, the formation of a thin protective superficial passive layer was observed, which increased in thickness due to ionic transfer through the film. Although an anodic solution associated with the passive layer was also created, in that region, the increase in polarization did not produce an increase in current density [31]. For the TiO<sub>2</sub> coatings evaluated with loads of 1 N, 2 N, and 5 N, a slight decrease in the current density was observed at 100 mV vs. Ag/AgCl; this can be attributed to the gradual growth process of the film and subsequent loss (instantaneous) after a critical time.

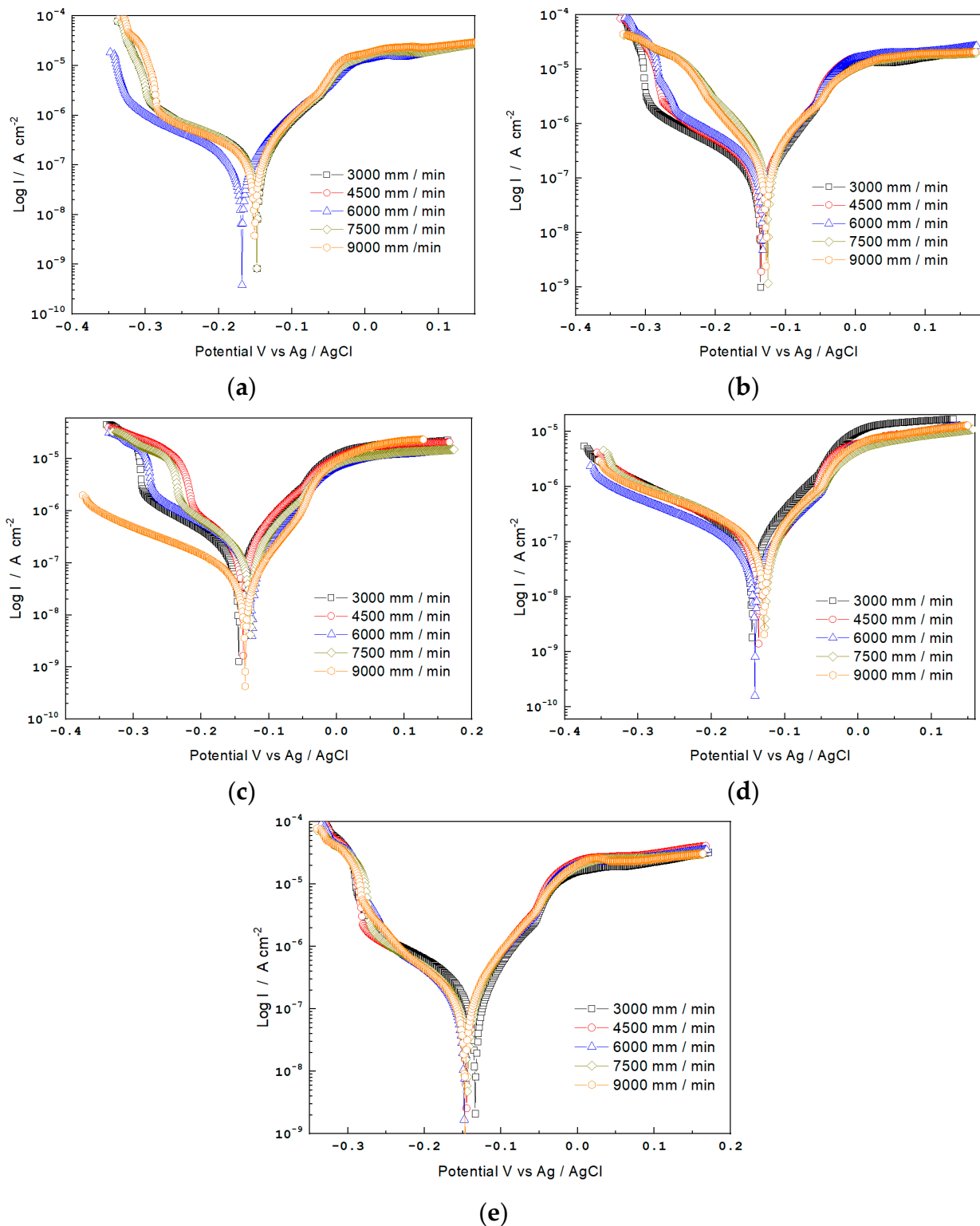


**Figure 6.** Potentiodynamic polarization curves of  $\text{TiO}_2$  coatings evaluated at different loads. (a) 1 N, (b) 2 N, (c) 3 N, (d) 4 N, and (e) 5 N.

Wear and corrosion are also present as destructive mechanisms that affect the useful life of coatings. In this study, it was observed that increasing the sliding speed and the load gave greater resistance to corrosion due to the absence of grain boundaries. These grain boundaries are responsible for generating points with high free energy levels that are prone to corrosion [32]. Varying the loads that are applied to the samples causes wear

and the formation of harmful particles, impacting the excellent performance of the coating system. Additionally, if the coatings are exposed to body fluids, they oxidize, generating corrosion products which, when added to the wear products, affect the deposited material and cause fractures.

The results showed a decrease in the corrosion rate as the load applied to the coating increased. At loads of 1 N, the value of the corrosion rate increased more than double concerning the other loads evaluated. The corrosion rate values were higher for sliding speeds between 3000 mm/min and 4500 mm/min at a load of 1 N due to the release of ions from the films. At loads of 1 N (Figure 7a), no tribo-films were formed. This behavior is related to the non-passivation of the metal [33].

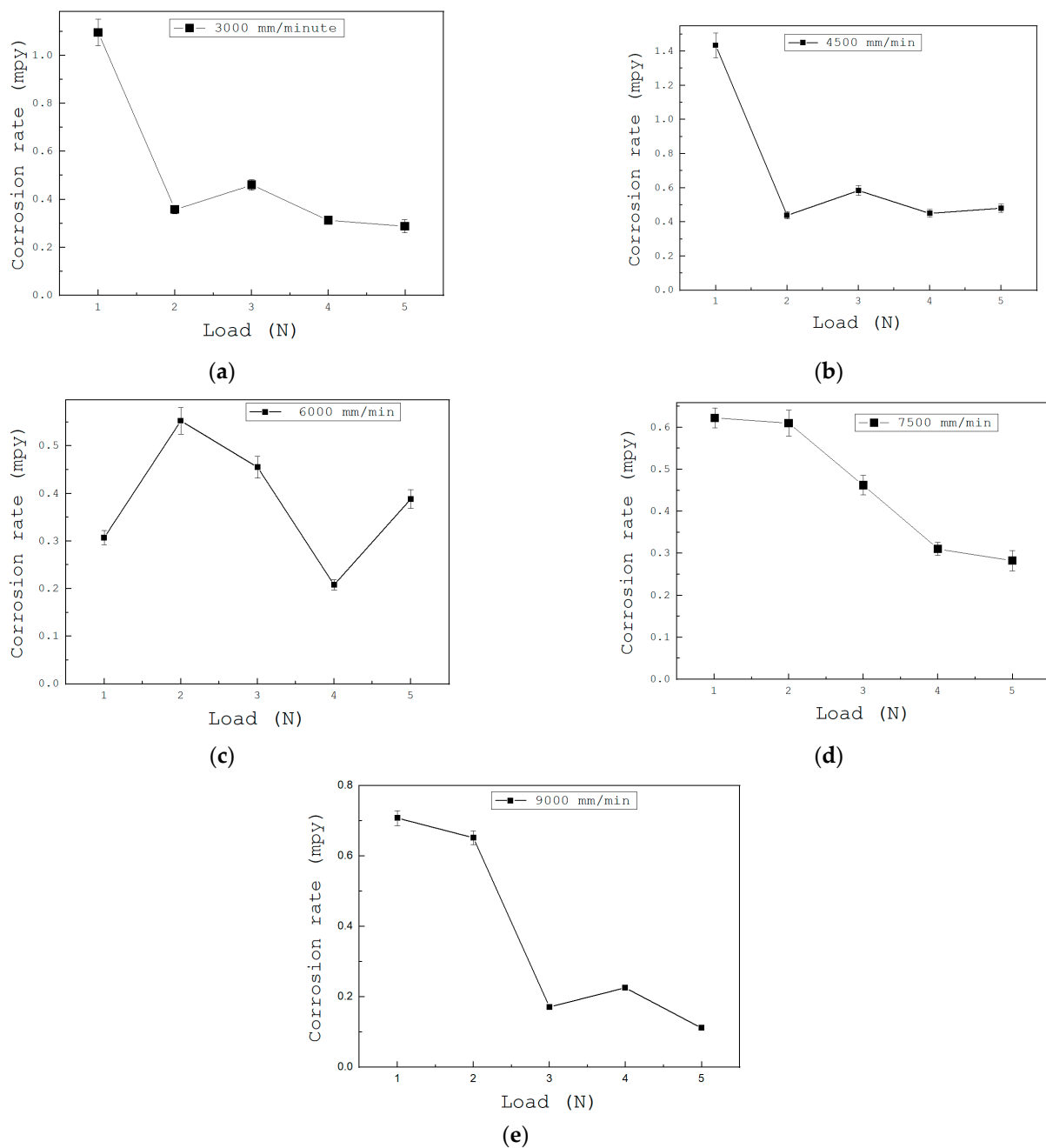


**Figure 7.** Variation in the corrosion rate as a function of the load applied to the system and the sliding rate. (a) 3000 mm/min, (b) 4500 mm/min, (c) 6000 mm/min, (d) 7500 mm/min, and (e) 9000 mm/min.



Figure 7 shows graphs of the corrosion rate, which can be related to weight loss as a function of distance. It can be observed that the corrosion rate increases in proportion to the test time [34]. The *Corrosion rate* was determined using Equation (1).

$$\text{Corrosion rate} = \frac{KW\beta_a\beta_c}{(2.303)AD(\beta_a + \beta_c)} \frac{1}{R_p'} \quad (1)$$

$K$  = a constant.

$W$  = mass loss in g.

$A$  = area in  $\text{cm}^2$ .

$D$  = density in  $\text{g}/\text{cm}^3$ .

In general, it is observed that the effect of the load applied to the coatings is inverse to the results for the corrosion rate. At loads of 1 N and speeds of 3000 mm/min and 4500 mm/min, the values of corrosion speeds produced the highest results for all the systems evaluated. This behavior indicates that slip velocities influence the coating's corrosion current density ( $i_{\text{corr}}$ ). The corrosion current density decreases at higher sliding speeds (6000 mm/min, 7500 mm/min, and 9000 mm/min) [35]. The low values in the corrosion current density suggest the generation of a pseudo-passive film. Notably, the 6000 mm/min speed obtained an  $i_{\text{corr}}$  value of approximately 0.03072 mpy, which is three-fold lower than that found for the coating at 4500 mm/min.

For loads of 2 N (Figure 7b), the wear was very similar to the results found for loads of 1 N. However, the maximum values in corrosion rate (0.06100 mpy) were observed at sliding speeds of 7500 mm/min. For the other slip velocities, values were found in a range from 0.045 mpy to 0.055 mpy. It is essential to highlight that at low sliding speeds, a minimum corrosion rate value of 0.03579 mpy was found due to the re-passivation process at the end of the run. The differences found for loads of 1 N in the re-passivation process were related to the plastic deformation of the coating.

For loads of 3 N (Figure 7c), the average corrosion rate values were 0.045 mpy for the range of sliding speeds. For example, at 4500 mm/min, the corrosion rate was 0.05836 mpy; for 9000 mm/min, all the tests' lowest current density values were obtained. Under these parameters, the corrosion rate was 0.01710 mpy.

Regarding the study applying loads of 4 N (Figure 7d), the results show that the electrochemical parameters remained constant. However, a slight increase in the corrosion rate was observed at 4500 mm/min, which may be related to an accumulation of corrosion products or substrate passivation [36].

For loads of 5 N (Figure 7e), a decrease in the corrosion rate was observed when the sliding rate increased. The results established that these load conditions favored the system's protection because there was no evidence of an increase in the corrosive processes produced by the saline solution and continuous movement.

Figure 8 shows the wear rates of the coatings as a function of the applied load and the sliding speed. As shown, the trend for the change in wear rates is similar to the corrosion rate; that is, it decreases as the applied load on the coatings increases. The estimated minimum values were  $1.37 \times 10^{-10} \text{ mm}^3/\text{N mm}$  for loads of 5 N at a sliding speed of 9000 mm/min, which is an improvement compared to those subjected to loads of 1 N. This behavior was also evident for coatings with loads of 3 N and 4 N and wear rates of  $1.71 \times 10^{-10} \text{ mm}^3/\text{N}$  a 9000 mm/min y  $2.07 \times 10^{-10} \text{ mm}^3/\text{N mm}$  at 6000 mm/min, respectively. The wear rate results indicate that the surface wear of the coatings could occur at low loads 1 N and 2 N and was related to adhesion phenomena and the production of abrasive particles causing abrasive wear. The abrasive particles come from the formation of oxides in the substrate, which, when delaminated on the surface, promote abrasive wear. Although wear rates are low, the gold coating acts as a protective layer preventing the formation of abrasive particles and surface wear of this coating. Although for loads of 3 N, 4 N, and 5 N, the wear rates were initially low, the difference lay in the sliding speed because speeds greater than 6000 mm/min was necessary to reach the state of wear in equilibrium and was related to the reduction in the wear on the surface of ceramic

coatings. This result suggests that the present wear mechanisms differ for the lower sliding loads and speeds (3000 mm/min and 4500 mm/min). As the sliding speed increased, the local temperature increased due to the sliding of the pin against the coating surface. The asperities and particles observed by atomic force microscopy (Figure 5) are oxides that determined that anodic zones provided greater resistance so that movement could occur, generating lower values of wear rates.

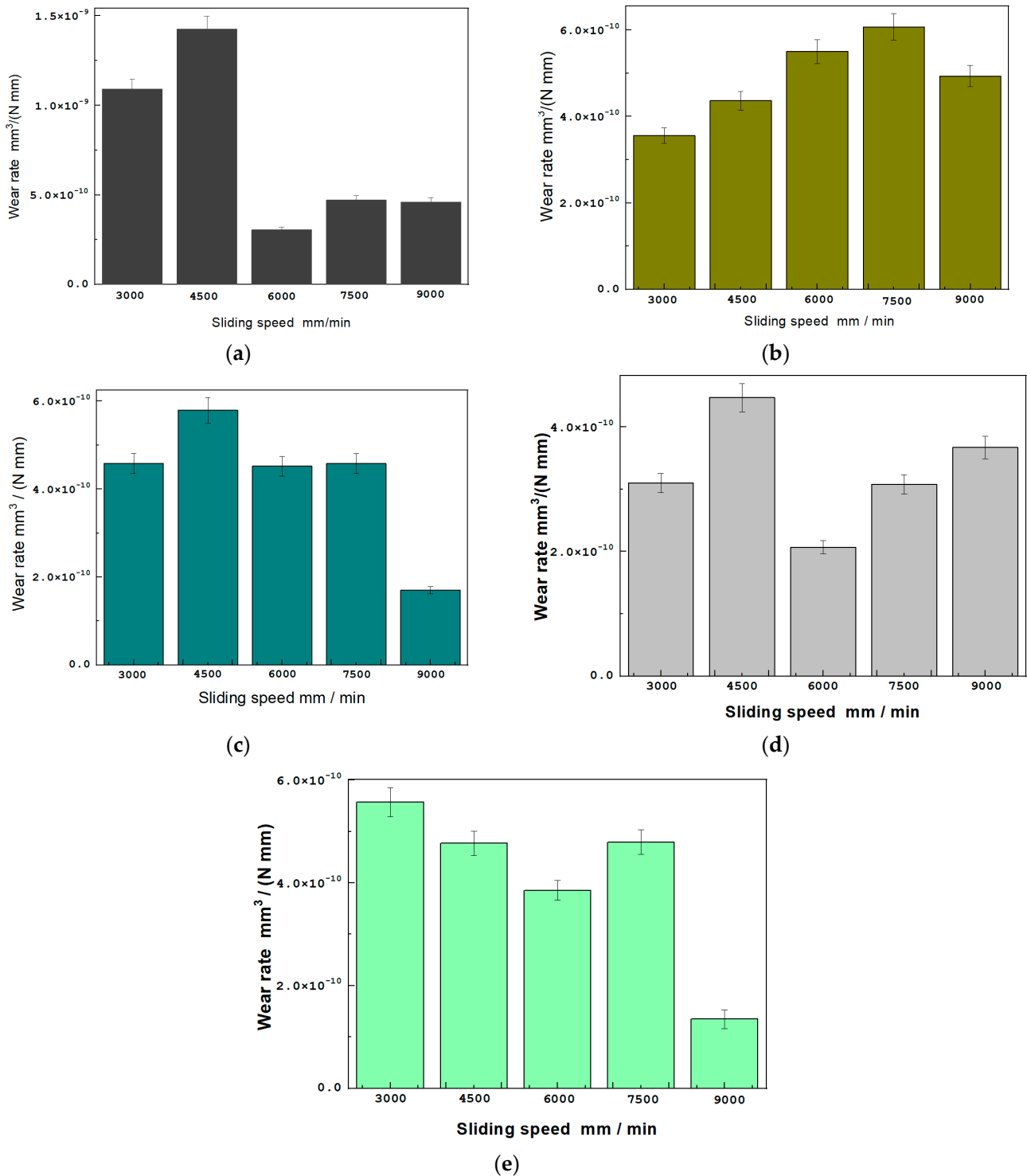


**Figure 8.** Rate of wear as a function of loads and sliding speeds. (a) 1 N, (b) 2 N, (c) 3 N, (d) 4 N, and (e) 5 N.

Sliding wear under tribocorrosive conditions is related to the adhesion tendency because of the applied load and chemical reactivity concerning sliding velocities that influence the current density. Figure 9a shows the impact of 1 N and 2 N loads for sliding speeds between 3000 mm/min and 4500 mm/min. The result is a tendency for plastic deformation due to the transfer of oxide particles from dissolved or solid corrosion products [37]. Figure 9b associates the effect of increasing the load to 3 N. When the coating surface comes into contact with the aqueous medium, thermodynamic and kinetic processes are initiated which are responsible for the formation of an electrochemical interface, and generate ductility, thus decreasing the wear rate, especially at a sliding speed of 9000 mm/min. Figure 9c corresponds to the results obtained for 5 N loads with low wear rates. Wear resistance varies by magnitude depending on the operating conditions during sliding contact.

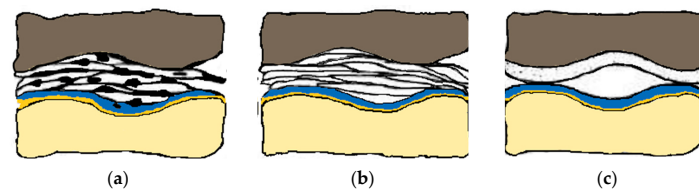


**Figure 9.** Types of wear generated by the interaction of the load and sliding speed. (a) The presence of particles in the fluid due to the adhesion generated by the loads and the roughness of the material, (b) Lower presence of particles due to the ductility of the coating, (c) Strongly attached ductile layers due to the chemical reaction assisted by the mechanical part.

Figure 10 shows the scanning electron microscopy images of the tracks in the coatings at 1 N, 2 N, 3 N, 4 N, and 5 N loads for sliding speeds at low speeds (3000 mm/min) and high speeds (9000 mm/min). The results show differences in terms of the morphology of the wear track depending on the applied load. For 1 N (Figure 10a,b) and 2 N (Figure 10c,d) loads, a more significant accumulation of fragments inside was observed in the wear pattern at low speeds and at the sides of the tracks. This coating did not suffer damage and plastic deformations in the form of grooves due to an increased temperature because of tribological contact when carrying out the wear tests. For 3 N loads (Figure 10e,f), similar results to those indicated above (1 N and 2 N loads) were observed. The only appreciable difference is the smaller size of the wear track. There are no grooves or deformations that can be related to good anti-wear behavior. Regarding the results found for loads of 4 N (Figure 10g,h) and 5 N (Figure 10i,j), it was determined that at high sliding speeds, the pin would not generate the central groove. Therefore, it is possible to affirm that the evaluated coatings provided greater resistance to wear and low wear rates.

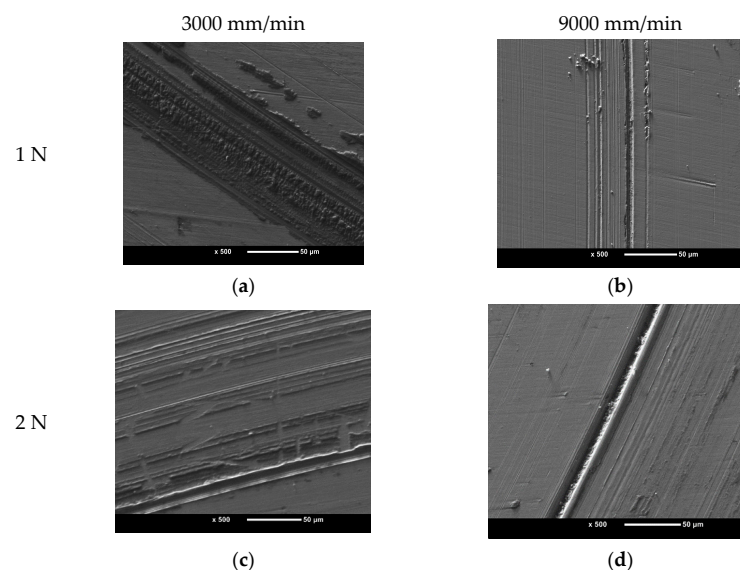


**Figure 10.** *Cont.*

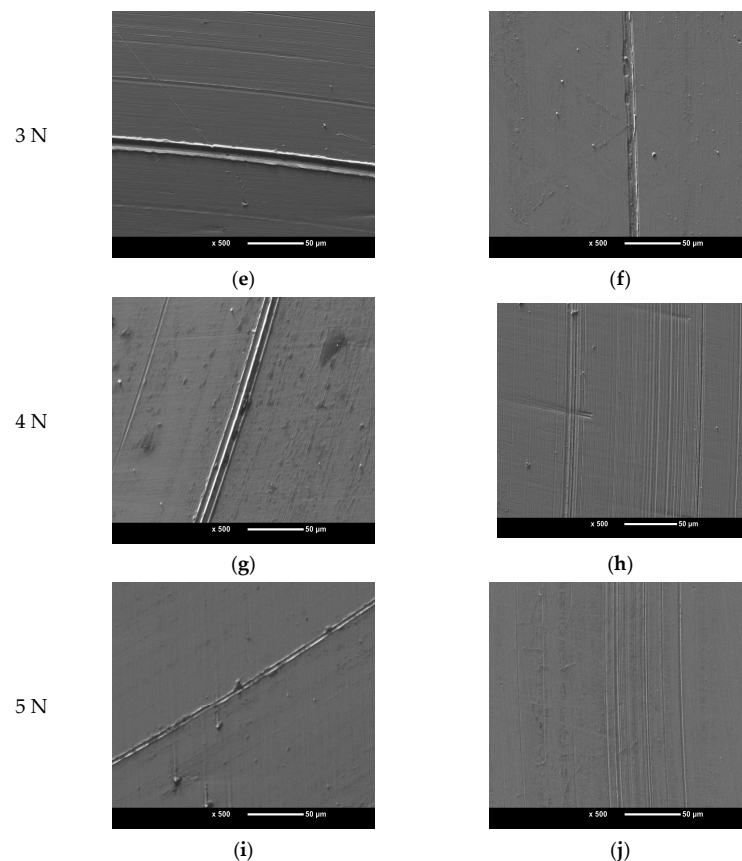


**Figure 10.** Trace of wear as a function of loads and sliding speeds. (a,b) 1 N, (c,d) 2 N, (e,f) 3 N, (g,h) 4 N, and (i,j) 5 N.

#### 4. Conclusions

The titanium oxide and gold interlayer coatings were successfully deposited by r.f. magnetron sputtering on titanium substrates. Their crystallographic, morphological, tribological, and electrochemical properties were determined.

The tribocorrosive behavior of nanostructured titanium oxide composites with a gold intermediate layer was evaluated as an average load and sliding velocity function. The study determined the increased resistance to tribocorrosion at higher loads and sliding speeds. The results indicate that the resistance was almost the same between the loads and low speeds associated with the increase in the real contact area and the tendency for adhesion. This conclusion is based on the wear rates of the coatings experienced in each charge.

The structural characterization of the gold and TiO<sub>2</sub> compound was obtained by including an intermediate layer of gold in the system.

The topography was modified depending on the manufacturing parameters of coatings, the interface layer of gold, and the TiO<sub>2</sub> superficial layer.

The films showed the growth of small superficial grains with size variation for the intermediate layer. Gold films were affected by the type of substrate and the deposition temperature. The application of TiO<sub>2</sub> layers favored the nucleation of larger and more homogeneous surface grains.

The influence of the load applied to the coatings; the slip speed on the tribological and electrochemical response was determined dually. Through the potentiodynamic polarization curves, an increase in the corrosion rate was observed at loads of 1 N and 2 N. The trend in corrosion resistance values at sliding speeds between 3000 mm/min and 4000 mm was also determined. Loads of 3 N, 4 N, and 5 N positively affected the wear and electrochemical properties (corrosive), and a significant decrease in the rate of

deterioration was observed. It is clear that increasing the pin slip speed positively affected the tribo-electrochemical properties.

With the results obtained, it was possible to determine the material's useful life. In addition, this information allowed us to know the material through the operation time. It is possible to predict the type of wear and areas of greater affectation due to the effect of the load depending on the corrosion mechanisms.

The most significant limitation of this developed work was optimizing the deposition process by modifying variables such as gas flow (Ar and O<sub>2</sub>), polarization voltage, working pressure, and power density to obtain multilayer coatings with thicknesses close to 3 μm, which could be implemented in implantology.

In the next phase of this research, biocompatibility tests of the obtained coatings are required, and the information regarding osteoblastic differentiation and bacterial resistance needs to be evaluated. Therefore, TiO<sub>2</sub> has the necessary surface morphology to modify orthopedic implants.

**Author Contributions:** Conceptualization, W.A. and J.B.-R.; methodology, J.S.-M.; software, W.A.; validation, J.B.-R.; formal analysis, J.S.-M.; investigation, W.A. and J.B.-R. All authors have read and agreed to the published version of the manuscript.

**Funding:** This research received no external funding.

**Acknowledgments:** W. Aperador and authors acknowledges the Universidad Militar Nueva Granada.

**Conflicts of Interest:** The authors declare no conflict of interest.

## References

1. Sahlin, H.; Contreras, R.; Gaskill, D.F.; Bjursten, L.M.; Frangos, J.A. Anti-inflammatory properties of micropatterned titanium coatings. *J. Biomed. Mater. Res.* **2006**, *77*, 43–49. [[CrossRef](#)] [[PubMed](#)]
2. Contreras, R.; Sahlin, H.; Frangos, J.A. Titanate biomaterials with enhanced antiinflammatory properties. *J. Biomed. Mater. Res.* **2007**, *80*, 480–485. [[CrossRef](#)] [[PubMed](#)]
3. Ying, M.; Jianxin, D.; Zhihui, Z.; Qinghao, S. Enhanced wear resistance of AlTiN coatings by ultrasonic rolling substrate texturing. *Surf. Coat. Technol.* **2022**, *447*, 128841.
4. Lin-Chan, S.; Nielsen, D.H.; Yack, J.; Hsu, M.; Shurr, D. The effects of added prosthetic mass on physiologic responses and stride frequency during multiple speeds of walking in persons with transtibial amputation. *Arch. Phys. Med. Rehabil.* **2003**, *84*, 1865–1871. [[CrossRef](#)]
5. Racic, V.; Pavic, A.; Brownjohn, J. Experimental identification and analytical modelling of human walking forces: Literature review. *J. Sound Vib.* **2009**, *326*, 1–49. [[CrossRef](#)]
6. Abadi, F.; Ariffin Muhamad, T.; Salamuddin, N. Energy Expenditure through Walking: Meta-Analysis on Gender and Age. *J. Sound Vib.* **2010**, *7*, 512–521. [[CrossRef](#)]
7. Skjöldebrand, C.; Joanne, L.; Hatto, P.; Bryant, M.; Hall, R.; Persson, C. Current status and future potential of wear-resistant coatings and articulating surfaces for hip and knee implants. *Mater. Today* **2022**, *15*, 100270. [[CrossRef](#)]
8. Saitoh, S.; Nezu, T.; Sasaki, K.; Taira, M.; Miura, H. Effect of gold deposition onto titanium on the adsorption of alkanethiols as the protein linker functionalizing the metal surface. *Dent. Mater. J.* **2014**, *33*, 111–117. [[CrossRef](#)]
9. Visai, L.; De Nardo, L.; Punta, C.; Melone, L.; Cigada, A.; Imbriani, M.; Arciola, C.R. Titanium oxide antibacterial surfaces in biomedical devices. *Int. J. Artif. Organs* **2011**, *34*, 929–946. [[CrossRef](#)]
10. Albrektsson, T.; Johansson, C. Osteoinduction, osteoconduction and osseointegration. *Eur. Spine J.* **2001**, *10*, 96–101.
11. Csarnovics, I.; Hajdu, P.; Biri, S.; Hegedűs, C.; Kökényesi, S.; Rácz, R.; Csik, A. Preliminary studies of creation of gold nanoparticles on titanium surface towards biomedical applications. *Vacuum* **2016**, *126*, 55–58. [[CrossRef](#)]
12. Heo, D.N.; Ko, W.K.; Lee, H.R.; Lee, S.J.; Lee, D.; Um, S.H.; Lee, J.H.; Woo, Y.H.; Zhang, L.G.; Lee, D.W.; et al. Titanium dental implants surface-immobilized with gold nanoparticles as osteoinductive agents for rapid osseointegration. *J. Colloid Interface Sci.* **2016**, *469*, 129–137. [[CrossRef](#)] [[PubMed](#)]
13. Wang, Z.; Zhang, J.; Hu, J.; Yang, G. Gene-activated titanium implants for gene delivery to enhance osseointegration. *Biomater. Adv.* **2022**, *143*, 213176. [[CrossRef](#)]
14. Oros-Ruiz, S.; Pedraza-Avella, J.A.; Guzmán, C. Effect of Gold Particle Size and Deposition Method on the Photodegradation of 4-Chlorophenol by Au/TiO<sub>2</sub>. *Top. Catal.* **2011**, *54*, 519–526. [[CrossRef](#)]
15. Jang, D.; Yu, S.; Chung, K.; Yoo, J.; Marques-Mota, F.; Wang, J.; Ahn, D.J.; Kim, S.; Kim, D.H. Direct deposition of anatase TiO<sub>2</sub> on thermally unstable gold nanobipyramid: Morphology-conserved plasmonic nanohybrid for combinational photothermal and photocatalytic cancer therapy. *Appl. Mater. Today* **2022**, *27*, 101472. [[CrossRef](#)]

16. Khung, R.; Sukjai-Suansuwan, N. Effect of gold sputtering on the adhesion of porcelain to cast and machined titanium. *J. Prosthet. Dent.* **2013**, *110*, 41–46. [[CrossRef](#)]
17. Shekhawat, D.; Singh, A.; Banerjee, M.K.; Singh, T.; Patnaik, A. Bioceramic composites for orthopaedic applications: A comprehensive review of mechanical, biological, and microstructural properties. *Ceram. Int.* **2021**, *47*, 3013–3030. [[CrossRef](#)]
18. Moghadasi, K.; Syahid, M.; Ashraf, M.; Zulhiqmi, M.; Raja, S.; Wu, B.; Yamani, M.; Ridha, B.M.; Yusof, F.; Fadzil, M.; et al. A review on biomedical implant materials and the effect of friction stir based techniques on their mechanical and tribological properties. *J. Mater. Res. Technol.* **2022**, *17*, 1054–1121. [[CrossRef](#)]
19. Yang, J.; Bai, S.; Sun, J.; Wu, H.; Sun, S.; Wang, S.; Xu, D. Microstructural understanding of the oxidation and inter-diffusion behavior of Cr-coated Alloy 800H in supercritical water. *Corros. Sci.* **2023**, *211*, 110910. [[CrossRef](#)]
20. Yate, L.; Coy, E.; Gregurec, D.; Aperador, W.; Moya, S.; Wang, G. Nb–C Nanocomposite Films with Enhanced Biocompatibility and Mechanical Properties for Hard-Tissue Implant Applications. *ACS Appl. Mater. Interfaces* **2015**, *7*, 6351–6358. [[CrossRef](#)]
21. Oropeza, F.; Egdell, R. Control of valence states in Rh-doped TiO<sub>2</sub> by Sb co-doping: A study by high resolution X-ray photoemission spectroscopy. *Chem. Phys. Lett.* **2011**, *515*, 249–253. [[CrossRef](#)]
22. Köbl, J.; Fernández, C.; Augustin, L.; Kataev, E.; Franchi, S.; Tsud, N.; Pistonesi, C.; Pronsato, E.; Jux, N.; Lytken, O.; et al. Benzohydroxamic acid on rutile TiO<sub>2</sub>(110)—(1 × 1)—a comparison of ultrahigh-vacuum evaporation with deposition from solution. *Appl. Surf. Sci.* **2022**, *716*, 121955. [[CrossRef](#)]
23. Dumbuya, K.; Cabailh, G.; Lazzari, R.; Jupille, J.; Ringel, L.; Pistor, M.; Lytken, O.; Steinrück, H.-P.; Gottfried, J. Evidence for an active oxygen species on Au/TiO<sub>2</sub>(110) model catalysts during investigation with in situ X-ray photoelectron spectroscopy. *Catal. Today* **2012**, *181*, 20–25. [[CrossRef](#)]
24. Zheng, L.; Yuan, X. An investigation on the performance of gold layer-based cyanide-free HAuCl<sub>4</sub> electroplating process under different power conditions. *Mater. Today Commun.* **2022**, *31*, 103711. [[CrossRef](#)]
25. Alférez, F.; Olaya, J.; Bautista-Ruiz, J. Síntesis y evaluación de resistencia a la corrosión de recubrimientos de SiO<sub>2</sub>-TiO<sub>2</sub>-ZrO<sub>2</sub>-BiO<sub>2</sub> sobre acero inoxidable 316L producidos por sol-gel. *Bol. Soc. Esp. Ceram. Vidr.* **2018**, *57*, 195–206. [[CrossRef](#)]
26. Balarabe, B.Y.; Maity, P. Visible light-driven complete photocatalytic oxidation of organic dye by plasmonic Au-TiO<sub>2</sub> nanocatalyst under batch and continuous flow condition. *Colloids Surf. A Physicochem. Eng. Asp.* **2022**, *655*, 130247. [[CrossRef](#)]
27. Bazaka, O.; Bazaka, K.; Khanh, V.; Levchenko, I.; Jacob, M.; Estrin, Y.; Lapovok, R.; Chichkov, B.; Fadeeva, E.; Kingshott, P.; et al. Effect of titanium surface topography on plasma deposition of antibacterial polymer coatings. *Appl. Surf. Sci.* **2020**, *521*, 146375. [[CrossRef](#)]
28. Jun-Li, Y.; Wen, H.; Zhang, Q.; Adachi, Y.; Arima, E.; Kinoshita, Y.; Nomura, H.; Ma, Z.; Kou, L.; Tsukuda, Y.; et al. Stable contrast mode on TiO<sub>2</sub>(110) surface with metal-coated tips using AFM. *Ultramicroscopy* **2018**, *191*, 51–55.
29. Dong, P.; Zhang, Y.; Zhu, S.; Nie, Z.; Ma, H.; Liu, Q.; Li, J. First-Principles Study on the Adsorption Characteristics of Corrosive Species on Passive Film TiO<sub>2</sub> in a NaCl Solution Containing H<sub>2</sub>S and CO<sub>2</sub>. *Metals* **2022**, *12*, 1160. [[CrossRef](#)]
30. Madhusmita, M.; Arunachalam, N. Effects of electrophoretic deposited graphene coating thickness on the corrosion and wear behaviors of commercially pure titanium. *Surf. Coat. Technol.* **2022**, *450*, 128946.
31. Xu, Z.; Yate, L.; Qiu, Y.; Aperador, W.; Coy, E.; Jiang, B.; Moya, S.; Wang, G.; Pan, H. Potential of niobium-based thin films as a protective and osteogenic coating for dental implants: The role of the nonmetal elements. *Mater. Sci. Eng. C* **2019**, *96*, 166–175. [[CrossRef](#)] [[PubMed](#)]
32. Song, B.; Hua, Y.; Zhou, C.; Li, Y.; Yang, L.; Song, Z. Fabrication and anticorrosion behavior of a bi-phase TaNbHfZr/CoCrNi multilayer coating through magnetron sputtering. *Corros. Sci.* **2022**, *196*, 110020. [[CrossRef](#)]
33. Moreno, H.; Caicedo, J.C.; Amaya, C.; Cabrera, G.; Yate, L.; Aperador, W.; Prieto, P. Improvement of the electrochemical behavior of steel surfaces using a TiN[BCN/BN]<sub>n</sub>/c-BN multilayer system. *Diam. Relat. Mater.* **2011**, *20*, 588–595. [[CrossRef](#)]
34. Jiang, C.; Xiong, W.; Cai, W.; Zhu, Y.; Wang, Y. Preload loss of high-strength bolts in friction connections considering corrosion damage and fatigue loading. *Eng. Fail. Anal.* **2022**, *137*, 106416. [[CrossRef](#)]
35. Zhang, H.; Kim, T.; Swarts, J.; Yu, Z.; Su, R.; Liu, L.; Howland, W.; Lucadamo, G.; Couet, A. Nano-porosity effects on corrosion rate of Zr alloys using nanoscale microscopy coupled to machine learning. *Corros. Sci.* **2022**, *208*, 110660. [[CrossRef](#)]
36. Hu, C.; Xie, X.; Ren, K. A facile method to prepare stearic acid-TiO<sub>2</sub>/zinc composite coating with multipronged robustness, self-cleaning property, and corrosion resistance. *J. Alloys Compd.* **2021**, *882*, 160636. [[CrossRef](#)]
37. Zhang, P.; Liu, J.; Gao, Y.; Liu, Z.; Mai, Q. Effect of heat treatment process on the micro machinability of 7075 aluminum alloy. *Vacuum* **2023**, *207*, 111574. [[CrossRef](#)]

**Disclaimer/Publisher's Note:** The statements, opinions and data contained in all publications are solely those of the individual author(s) and contributor(s) and not of MDPI and/or the editor(s). MDPI and/or the editor(s) disclaim responsibility for any injury to people or property resulting from any ideas, methods, instructions or products referred to in the content.